Applied Catalysis B: Environmental 227 (2018) 376–385

Contents lists available at ScienceDirect

Applied Catalysis B: Environmental

journal homepage: www.elsevier.com/locate/apcatb

In-situ synthesis of direct solid-state dual Z-scheme WO_3/g-C_3N_4/Bi_2O_3 photocatalyst for the degradation of refractory pollutant

Longbo Jiang[a,b], Xingzhong Yuan[a,b,*], Guangming Zeng[a,b], Jie Liang[a,b,*], Xiaohong Chen[c], Hanbo Yu[a,b], Hou Wang[d], Zhibin Wu[a,b], Jin Zhang[a,b], Ting Xiong[a,b]

[a] College of Environmental Science and Engineering, Hunan University, Changsha 410082, PR China
[b] Key Laboratory of Environmental Biology and Pollution Control (Hunan University), Ministry of Education, Changsha 410082, PR China
[c] Mobile E-business 2011 Collaborative Innovation Center of Hunan Province, Hunan University of Commerce, Changsha 410205, China
[d] School of Chemical and Biomedical Engineering, Nanyang Technological University, 637459, Singapore

ARTICLE INFO

Keywords:
WO_3/g-C_3N_4/Bi_2O_3
Photocatalysis
Dual Z-scheme mechanism
Electron-hole separation
Tetracycline degradation

ABSTRACT

Artificial Z-scheme photocatalyst can not only reduce the recombination of photogeneraged electron–holepairs, but also retain prominent redox ability. In this study, direct solid-state dual Z-scheme WO_3/g-C_3N_4/Bi_2O_3 photocatalyst was successfully synthesized by one step co-calcination stratage using tungstic acid, melamine and bismuth (III) nitrate pentahydrate as the precursors. Surface, morphological, and structural properties of the resulting materials were comprehensive characterized by XRD, XPS, SEM, TEM, UV–vis diffuse reflection spectroscopy, BET surface areas, photoluminescence and ESR analysis. The WO_3/g-C_3N_4/Bi_2O_3 composite exhibited superior photocatalytic activities for tetracycline degradation than that of pure g-C_3N_4, WO_3, Bi_2O_3 and their binary composites under visible light irradiation. The enhanced photocatalytic performance of WO_3/g-C_3N_4/Bi_2O_3 composite can be ascribed to improved visible light absorption, increased surface area and enhanced separation efficiency of photo-generated electron-hole pairs. In addition, the photocatalyst exhibits high stability and reusability. On the basis of the results, a novel direct solid-state dual Z-scheme photocatalytic mechanism was also proposed.

1. Introduction

Semiconductor-based photocatalysis using solar energy has attracted increasing attention as a potential alternative technology for environmental protection and remediation [1–5]. In order to achieve the above goals, two problems must be resolved, i.e., extending the excitation wavelength range of photocatalysts and increasing the separation efficiency of photoinduced electron-hole pairs [6]. However, conventional photocatalysts, such as TiO_2 (band gap ≈3.2 eV), respond only to UV radiation, which comprises less than 5% of the solar spectrum. During past few decades, many metal oxides, metal sulfides, oxyhalides and organic semiconductor materials with efficient visible light response have been widely investigated [7–9]. As is known, single-component photocatalyst was always limited by the quick combination of photo-generated electrons and holes, which results in poor quantum efficiency and low photocatalytic activity [10]. To date, many efforts, such as non-metal doping, facet control, surface sensitization and heterojunction construction, have been applied to broaden the photoresponse window and limit the recombination of photogenerated carriers [1,11–17]. Among various approaches, heterojunction photocatalysts have been fabricated extensively to enhance the separation efficiency of photoexcited electron-hole pairs [18–21].

In general, when two semiconductors with the suitable band structures were coupled into a heterojunction photocatalyst, the photogenerated electrons and holes are transferred into conduction band (CB) and valence band (VB) of the coupled semiconductor respectively because of their potential difference of CB and VB [14,19,22]. However, the reducibility of photogenerated electrons and the oxidizability of photoexcited holes are lower after the charges transfer [23]. Recently, the construction of biomimetic artificial Z-scheme photocatalyst has attract more and more attention because it not only can reduce the recombination of photogeneraged electron–hole pairs, but also can retain prominent redox ability [23,24]. Up to now, various Z-scheme systems have been designed, such as Ag_2CO_3/Ag/WO_3 [25], $SrTiO_3$:La,Rh/Au/$BiVO_4$ [26], TiO_2/C_3N_4−(IO^{3-}/I^-) [27], (Ru/$SrTiO_3$:Rh)/($BiVO_4$)–(Fe^{3+}/Fe^{2+}) [28], CdS/rGO/g-C_3N_4 [29], Bi_2MoO_6/CNTs/g-C_3N_4 [30], As described above, the present Z-scheme systems usually had noble metal (Ag, Au) [25,26], carbon materials

* Corresponding authors at: College of Environmental Science and Engineering, Hunan University, Changsha, 410082, PR China.
E-mail addresses: yxz@hnu.edu.cn (X. Yuan), liangjie@hnu.edu.cn (J. Liang).

https://doi.org/10.1016/j.apcatb.2018.01.042
Received 10 October 2017; Received in revised form 29 December 2017; Accepted 18 January 2018
Available online 31 January 2018
0926-3373/

[29,30] or redox pair (Fe^{3+}/Fe^{2+}, IO^{3-}/I^{-}) [27,28], leading to relative high cost and low stability of these photocatalysts for practical application. Thus, direct Z-scheme photocatalytic system has become a hotspot of research for application in environmental remediation [23,31–33].

Recently, metal-free graphitic carbon nitride (g-C_3N_4) has attracted intensive attention for the applications in photocatalytic organic pollutant degradation, water splitting, CO_2 reduction and organic synthesis under visible light [34–36]. In detail, g-C_3N_4 is a medium band gap (~2.7 eV) semiconductor with good visible light response (up to 460 nm) and high stability [37]. Generally, the VB position (E_{VB}) of g-C_3N_4 is about 1.57 eV, and the CB position (E_{CB}) is about −1.13 eV [29,38]. However, the pristine g-C_3N_4 is usually limited by unsatisfactory photocatalytic efficiency due to the insufficient visible light absorption, low surface area and the fast recombination of photoexcited electron-hole charges [39,40]. As mentioned above, the construction of direct Z-scheme heterojunction with matched VB and CB is benefit for enhancing the separation efficiency and promoting the redox ability. Successful cases, such as CeO_2/g-C_3N_4 [41], TiO_2/C_3N_4 [27], BiOI/g-C_3N_4 [42], Bi_2O_3/g-C_3N_4 [32], WO_3/g-C_3N_4 [6], Ag_3PO_4/g-C_3N_4 [43], $BiVO_4$/g-C_3N_4 [31], and so on. Nowadays, most efforts of Z-scheme photocatalysts have been devoted on binary composites. However, these binary systems were always impeded by the limited visible light response and relatively low charge separation efficiency [22,44]. Recently, the fabrication of g-C_3N_4 based Z-scheme ternary composites by combing conducting materials, co-catalyst, and another semiconductor has attracted great attention as a promising approach to further enhance visible light absorption, create faster charge carrier separation and facilitate effective redox reactions [29,45–47]. For example, Jo and Natarajan prepared Z-scheme $ZnIn_2S_4$/g-C_3N_4/$BiVO_4$ nanorod-based ternary nanocomposite photocatalysts with enhanced visible light absorption, high surface area, high adsorption capacity, and increased charge lifetime [47].

Tungsten oxide (WO_3) is regarded as a promising semiconductor material with narrow band gap (2.7 eV) and good stability [6]. Similarly, bismuth oxide (Bi_2O_3) is another important metal oxide semiconductor with a direct band gap of 2.8 eV [32]. It is known that the E_{CB} of WO_3 is about 0.74 eV and the E_{VB} is about 3.44 eV [6]. Furthermore, the E_{CB} of Bi_2O_3 is about 0.33 eV, and the E_{VB} is 3.13 eV [32]. Therefore, the hole generated on the VB of both WO_3 and Bi_2O_3 has a strong oxidative capability that is similar to TiO_2. Moreover, the more positive CB level of both WO_3 and Bi_2O_3 makes the generated electron has a limited reductive ability than of TiO_2. However, their efficiencies under visible light still need to be improved duo to the fast recombination of photogenerated charge carriers. According to the literatures, Bi_2O_3/g-C_3N_4 and WO_3/g-C_3N_4 composites have been reported to exhibit much enhanced photocatalytic activity by heterojunctions or Z-scheme mechanism [6,32,48,49]. However, the light absorption and the charge transfer rate of Bi_2O_3/g-C_3N_4 and WO_3/g-C_3N_4 composites still need to be improved. Fortunately, all the WO_3, Bi_2O_3 and g-C_3N_4 can be obtained by a similar calcination stratage [6,49,50].

Herein, a direct dual Z-scheme photocatalyst WO_3/g-C_3N_4/Bi_2O_3 exhibiting excellent photocatalytic activity was synthesized by one step co-calcination stratage in this study. The photocatalytic performance of WO_3/g-C_3N_4/Bi_2O_3 was evaluated by the degradation of tetracycline (TC) under visible light irradiation. The as-prepared WO_3/g-C_3N_4/Bi_2O_3 composite exhibited much better photocatalytic performance than that of pure g-C_3N_4, WO_3, Bi_2O_3 and their binary composites under visible-light irradiation ($\lambda > 420$ nm). The origin of enhanced photoactivity for WO_3/g-C_3N_4/Bi_2O_3 composites was explored by thorough investigation of structure, morphology and optical properties. Furthermore, a novel direct solid-state dual Z-scheme photocatalytic mechanism for was also proposed.

2. Experimental

2.1. Materials

Melamine and bismuth (III) nitrate pentahydrate ($Bi(NO_3)_3$ $5H_2O$) were purchased from Sinopharm Chemical Reagent Co., Ltd. Tungstic acid (H_2WO_4) and tetracycline hydrochloride (TC) was supplied by Aladdin Chemistry Co. Ltd. All chemicals were of analytical reagent grade and used without further purification.

2.2. Synthesis of WO_3/g-C_3N_4/Bi_2O_3 composite

g-C_3N_4 was prepared according to a widely used procedure [32]. In detail, 5 g melamine powder was and calcined at 520 °C for 2 h in an alumina crucible with a cover, then increased to 540 °C for another 2 h. After cooling down to room temperature, the obtained yellow product was milled into powder for further use. Pure WO_3 and Bi_2O_3 was prepared using the same calcination method, which used tungstic acid and bismuth (III) nitrate pentahydrate as the precursor, respectively.

The preparation of WO_3/g-C_3N_4/Bi_2O_3 photocatalyst was as follows: typically, 4.0 g melamine, 0.1 g H_2WO_4 and 0.1 g $Bi(NO_3)_3{\cdot}5H_2O$ were added into an agate mortar and grounded together. The obtained powders were heated as described above. Briefly, they were calcined at 520 °C for 2 h in an alumina crucible with a cove, then increased to 540 °C for another 2 h. After cooled down to room temperature, the resulted product was milled into powder and labeled as WCB. As comparison, binary composites WO_3/Bi_2O_3, g-C_3N_4/Bi_2O_3, g-C_3N_4/WO_3 were prepared with the same procedure without melamine, H_2WO_4 and $Bi(NO_3)_3{\cdot}5H_2O$, respectively. The obtained samples were milled into powder and labeled as WB, CB and CW, respectively.

2.3. Characterization

Powder XRD analysis was conducted by Bruker AXS D8 advance diffractometer operating with Cu-Ka source. Field emission scanning electron microscopy (SEM) (JSM-7001F, Japan) and transmission electron microscopy (TEM) (F20, USA) were used to examine the surface morphology. UV–vis diffuse-reflectance spectra (UV–vis DRS) were recorded with a Varian Cary 300 spectrometer equipped with an integrating sphere. The surface electronic state was analyzed by X-ray photoelectron spectroscopy (XPS) (Thermo Fisher Scientific, UK). The total organic carbon (TOC) data were obtained by a Shimadzu TOC-VCPH analyzer. N_2 absorption–desorption data (ASAP2020, Micromeritics, USA) was applied to characterize the specific surface area. Photoluminescence (PL) spectroscopy was measured on PerkinElmer LS-55 spectrofluorimeter at the excitation wavelength of 350 nm. The electron spin resonce (ESR) signals were examined on a Bruker ER200-SRC spectrometer under visible light irradiation ($\lambda > 420$ nm).

2.4. Photocatalytic evaluation

The photocatalytic performances of the obtained samples were investigated using 10 mg/L TC as pollutant. A 300 W Xenon lamp (Beijing China Education Au-light, Co., Ltd.) was used as the visible-light source ($\lambda > 420$ nm). The average visible light intensity was ca.100 mW cm^{-2} measured by a light meter (HS1010). Briefly, 100 mg photocatalyst was dispersed into 100 mL of TC. Prior to visible light irradiation, the suspension was magnetically stirred for 60 min in the dark to establish the adsorption–desorption equilibrium. At a certain time interval of irradiation, 4 mL suspension was taken out and filtrated through a 0.45 μm Millipore filter to remove the photocatalyst particles. The concentrations of TC were analyzed with an UV–vis spectrophotometer (UV-2250, SHIMADZU Corporation, Japan) at the characteristic absorption peak of 357 nm.

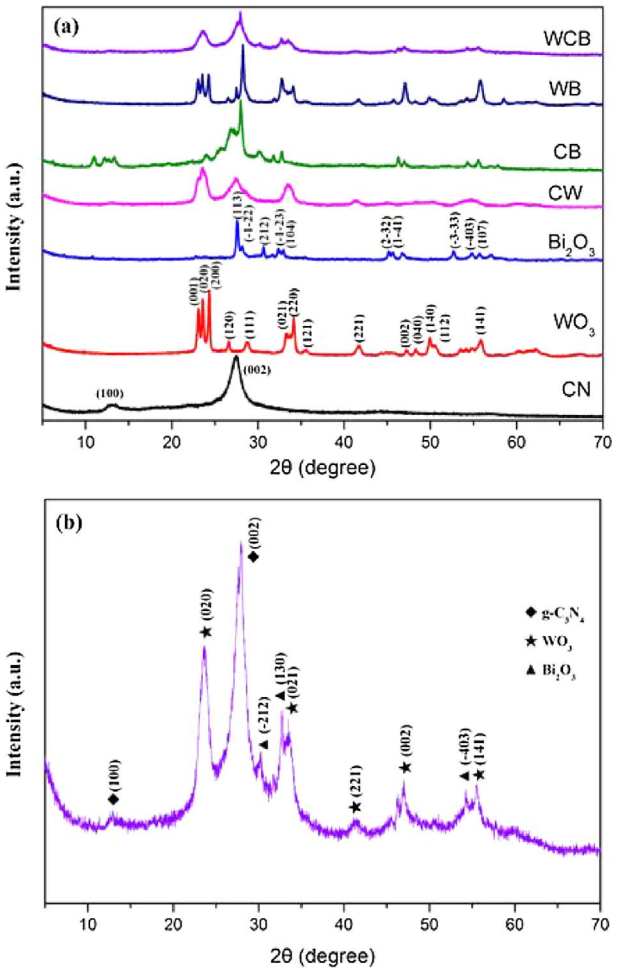

Fig. 1. (a) XRD patterns of the as-prepared samples; (b) The detailed information of WCB.

3. Results and discussion

3.1. XRD analysis

Fig. 1 depicts the XRD patterns of the as-prepared samples. It is obvious that the pure g-C_3N_4 had two peaks at 13.1° and 27.6°, which can be ascribed to (100) and (002) diffraction planes (JCPDS 87–1526), indicating the characteristic graphitic-like layered stacking of CN-based materials. For pure WO_3 sample, all the diffraction peaks were in good agreement with the standard monoclinic phase WO_3 (JCPDS 20–1324) [6,51]. Similarly, all the diffraction peaks of pure Bi_2O_3 can be readily indexed to the monoclinic structure of Bi_2O_3 (JCPDS 50–1088). The sharp diffraction peaks of both WO_3 and Bi_2O_3 indicate their good crystallinity. For binary composites WO_3/Bi_2O_3, g-C_3N_4/Bi_2O_3 and g-C_3N_4/WO_3, obviously, the peaks contained the characteristic peaks of each other. As for $WO_3/C_3N_4/Bi_2O_3$, the detailed characteristic peaks can be found in Fig. 1b. The characteristic diffraction peaks of monoclinic WO_3 and monoclinic Bi_2O_3 were obviously present in the XRD pattern of WO_3/g-C_3N_4/Bi_2O_3 curves. The XRD results of WCB also revealed the typical (100) and (002) diffraction planes of g-C_3N_4 (JCPDS 87–1526) at 2θ of 13.1° and 27.6°. This results indicated that the WO_3/g-C_3N_4/Bi_2O_3 was formed and no any other impurities.

3.2. Chemical states analysis

XPS spectra was conducted to reveal the surface elemental composition and chemical states of the WCB composite. Fig. 2 exhibited the survey of the obtained WCB hybrid and high-resolution XPS spectra of the C 1s, N 1s, O 1s, W 4f and Bi 4f. The XPS survey spectra (Fig. 2a) shows the existence of C, N, W, Bi, and O elements. Furthermore, the typical high-resolution XPS spectra of C 1s, N 1s, W 4f, Bi 4f and O 1s are conducted. As shown in Fig. 2b, C 1s peak at about 284.8 eV can be assigned the adventitious carbon depositing on the surface of photocatalyst. The major peak of C 1s at 288.1 eV is attributed to a sp^2-hybridized carbon in an N-containing aromatic ring (N−C═N) in the g-C_3N_4 lattice [52]. The N1s spectrum (Fig. 2c) in WCB hybrid can be deconvoluted into three peaks with binding energies at 398.8, 399.6, and 400.3 eV, corresponding to the C−N═C species, N–$(C)_3$ groups, and N−H bonds [53,54]. In the high resolution spectrum of W 4f (Fig. 2d), two peaks at 35.5 eV and 37.7 eV correspond to the characteristic W 4f 7/2 and W 4f 5/2 peaks for WO_3, respectively [55]. Fig. 2e shows the XPS spectra of Bi 4f, where the peaks at 164.8 and 159.5 eV can be correspond to Bi 4f 5/2 and 4f 7/2 spectra of Bi^{3+} in the WCB [56]. The O 1s spectrum in Fig. 2f exhibits the binding energy of 530.4 eV which is ascribed to the lattice oxygen in the WO_3 and Bi_2O_3 [57]. There, this results further confirm the co-existence of WO_3, Bi_2O_3, and g-C_3N_4 in the WCB heterostructures.

3.3. Morphology characterization

The morphology and microscopic structure of g-C_3N_4, WO_3, Bi_2O_3, and the obtained WCB composites were characterized by SEM, TEM, and HRTEM. Fig. 3a displays that g-C_3N_4 samples exhibited an aggregated, slate-like, and different nanosizes crystals stacking layers with smooth structures, which is the typical structure characteristic of g-C_3N_4 synthesized by the polymerization method [58,59]. It can be observed that the as-prepared WO_3 was mainly composed of square sheet-like structures (Fig. 3b). As shown in Fig. 3c, the obtained Bi_2O_3 exhibits flower-like sphere which is self-assembled by nanosheets. As for WCB, it can be seen that the composite is less smooth compared with pure g-C_3N_4 and some small particles coated on the surface of bulk g-C_3N_4 (Fig. 3d). In addition, TEM was further employed to investigate the detailed morphology. The results from TEM data are also consistent with the observation from SEM images (Fig. 3e and h). Particularly, it can be clearly observed that WO_3 nanoparticles and Bi_2O_3 spheres are randomly anchored on the surface of bulk g-C_3N_4 with high dispersion (Fig. 3h). High-resolution TEM (HR-TEM) was further employed to investigate the detailed crystal structure of the as-prepared samples. As depicted in Fig. 3i, pure g-C_3N_4 exhibited an amorphous structure [60]. Fig. 3 j and k indicated that the lattice spacings of 0.377 and 0.327 nm correspond to the (020) plane of WO_3 and (120) plane of the Bi_2O_3, respectively. Furthermore, the HRTEM of WCB displayed the typical (020) plane of WO_3, (120) plane of the Bi_2O_3 and amorphous g-C_3N_4, which confirmed the coexistence of WO_3, Bi_2O_3 and g-C_3N_4 phases (Fig. 3l). Additionally, EDS image of WCB composite was also performed, which verifies the presence of C, N, W, Bi and O elements (Fig. S1). The above results are consistent with the result of XRD and XPS. WO_3 and Bi_2O_3 were closely contacted with g-C_3N_4, which could be beneficial for the transfer of charges during the photocatalytic oxidation process through Z-scheme strategy. These further demonstrate that WO_3/g-C_3N_4/Bi_2O_3 dual Z-scheme photocatalysts are successfully fabricated by a facile co-calcination stratage.

3.4. Specific surface area and optical properties

The N_2 adsorption–desorption isotherms and the corresponding pore size distributions of the as-prepared samples are depicted in Fig. 4. Obviously, the samples display type IV isotherms with type H3 hysteresis loop, indicating that the samples have a mesoporous structure which has been confirmed by the pore size distributions shown in Fig. 4b [32,61]. The specific surface areas, pore sizes and pore volumes of the as-prepared photocatalysts calculated by BET and BJH methods are summarized in Table 1. Interestingly, the binary CW and ternary WCB composites exhibited much higher BET surface area and pore

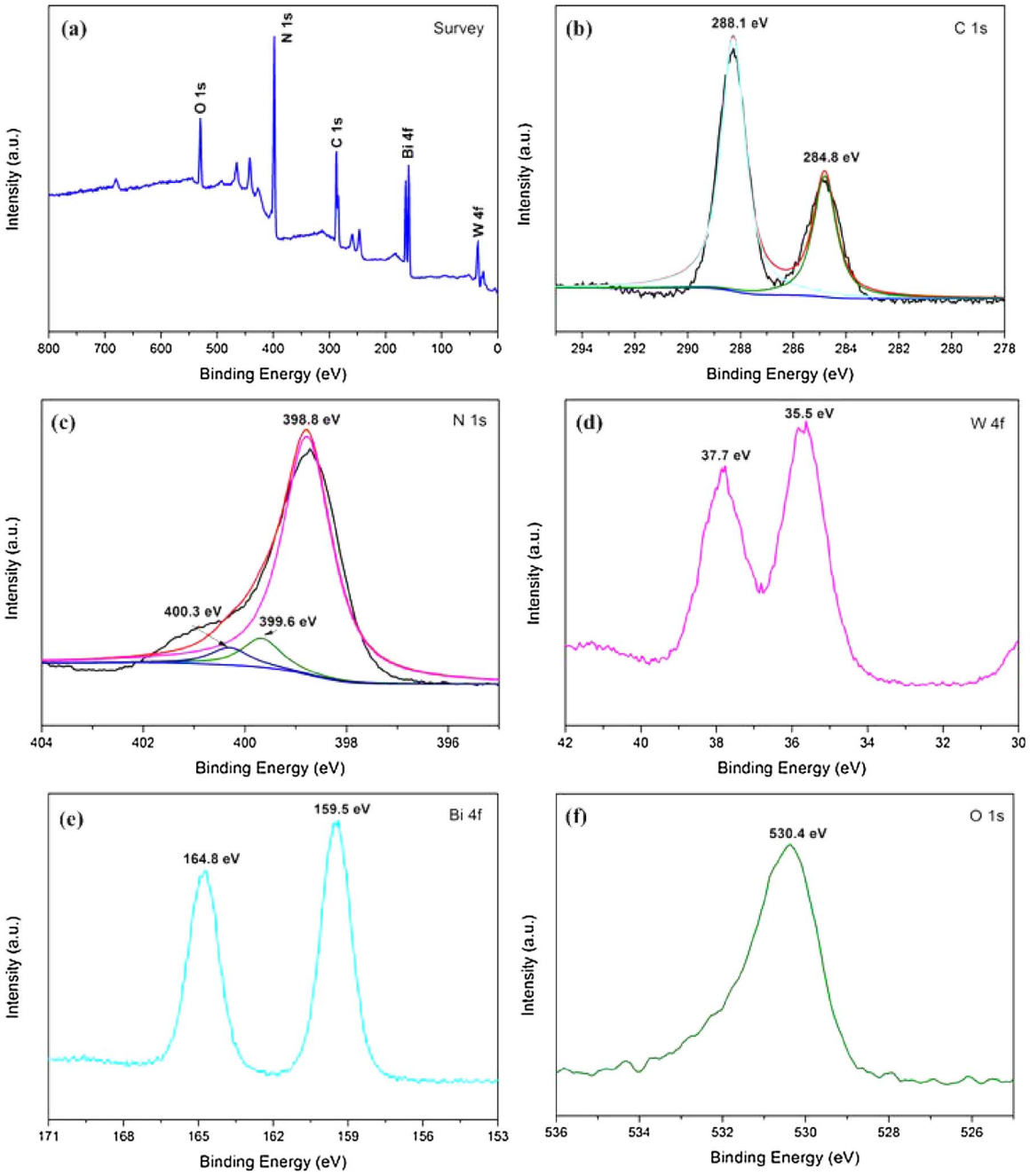

Fig. 2. XPS spectra of the WCB composite. (a) Survey of the sample; (b) C 1s; (c) N 1s; (d) W 4f; (e) Bi 4f and (f) O 1s.

volume than those of single WO_3, g-C_3N_4 and Bi_2O_3. It may be caused by that the formation of WO_3 nanoparticles between the interlayers of g-C_3N_4 sheets would make the g-C_3N_4 sheets unfold to increase the BET surface area and pore volume [49]. However, the S_{BET} of the WCB composite showed a slight decrease compared with the binary CW hybrid (Table 1). This may be caused by the addition of Bi_2O_3, which can be confirmed by the fact that CB displays a similar S_{BET} with g-C_3N_4. It is known that the higher specific surface areas can provide abundant active reaction sites and facilitate more pollutant molecules being adsorbed on its surface [2,62,63]. Thus, it can be concluded that the surface area contributed to the enhanced photocatalytic activities compared with single samples, but not the critical factor for higher removal efficiency compared with binary CB in this system.

The optical properties of as-prepared ternary and binary composites, as well as the single WO_3, g-C_3N_4 and Bi_2O_3 were characterized using UV−vis DRS. As depicted in Fig. 5, the pure g-C_3N_4 and WO_3 have an similar absorption edge at ~480 nm whereas Bi_2O_3 shows absrption edge at around 440 nm. It is obvious that Bi_2O_3 sample exhibited the strongest absorption in the ultraviolet light region ($\lambda < 420$ nm), while it almost has no obvious absorbance in the visible light region. As for WCB, the red shift and enhanced visible absorbance are observed, which may be attributed to the interaction among WO_3, g-C_3N_4 and Bi_2O_3. Because of the intensive absorptions in the visible region, the nanocomposites could have remarkable photocatalytic activity under the visible-light irradiation.

In general, the optical absorption band edge (E_g) of a semiconductor photocatalyst can be estimated according to the following formula:

$$\alpha h\nu = A(h\nu - E_g)^{n/2} \quad (1)$$

where α, h, v, E_g, and A are the absorption coefficient, Planck constant, light frequency, band gap energy, and a constant, respectively. The E_g of the WO_3, g-C_3N_4 and Bi_2O_3 were determined from a plot of $(\alpha h\nu)^{1/2}$

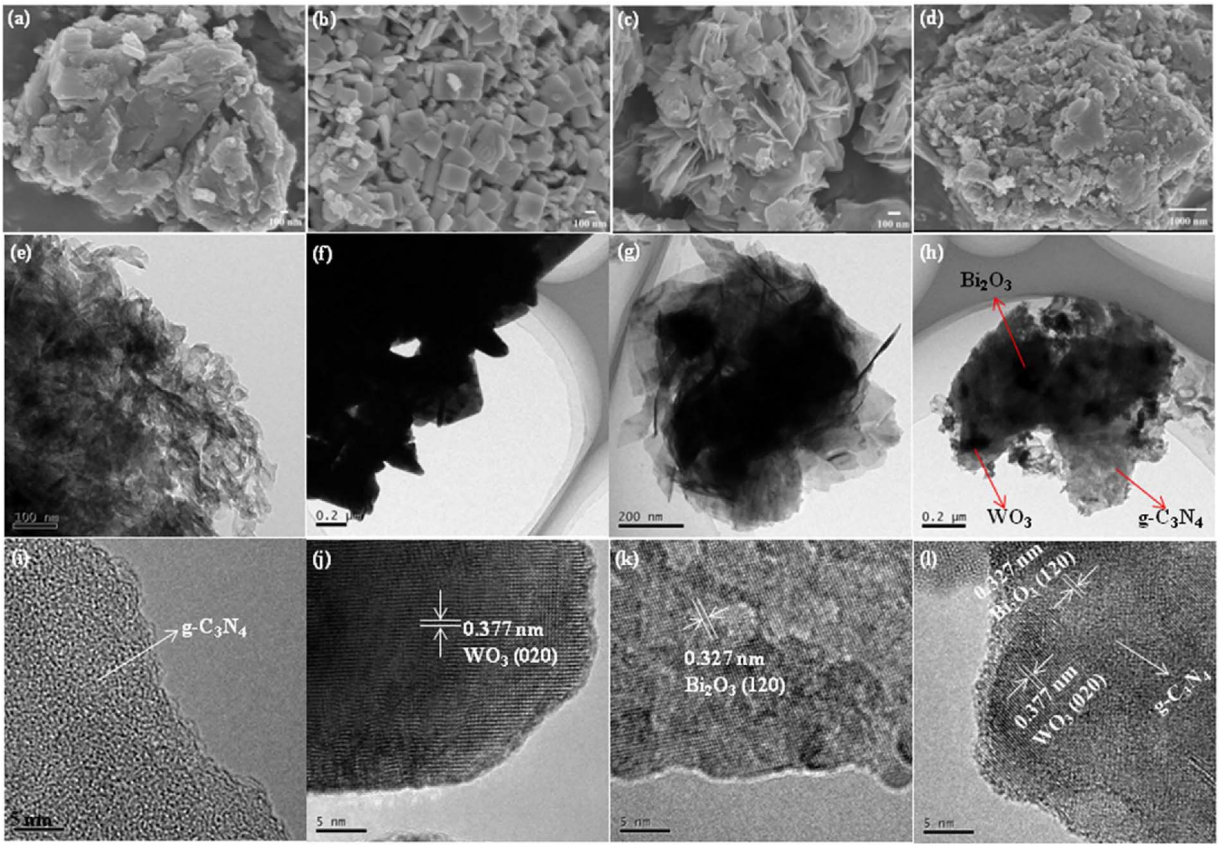

Fig. 3. SEM images of (a) g-C_3N_4, (b) WO_3, (c) Bi_2O_3, (d) WCB. TEM micrographs of (e) g-C_3N_4, (f) WO_3, (g) Bi_2O_3, (h) WCB. (d) high-resolution images of (i) g-C_3N_4, (j) WO_3, (k) Bi_2O_3, (l) WCB.

vs. hν (n = 4 for indirect transition). From the tangent line of the curve, extrapolated to the hν axis intercept, the bandgap of g-C_3N_4 was found to be 2.54 eV. Similarly, the bandgaps of WO_3 and Bi_2O_3 were estimated to be about 2.51 eV and 2.80 eV, respectively. The band gap of WCB is slight smaller than the single samples, which is consistent with the enhanced light absorption.

Generally, the charge separation and migration always significantly affect the photocatalytic performance. Photoluminescence (PL) spectra is applied to explore the migration and recombination process of photoexcited carries in this study [3,51]. The lower PL emission intensity indicates the lower recombination efficiency of the photoinduced electron-hole pairs and determines the higher photocatalytic performance [57,64]. Fig. 6 exhibited the PL spectra of pure g-C_3N_4, WO_3,

Table 1
BET surface areas, pore diameter and pore volumes of the as-prepared samples.

Photocatalysts	S_{BET} ($m^2 g^{-1}$)	Pore diameter (nm)	Pore volume ($cm^3 g^{-1}$)
g-C_3N_4	6.05	18.08	0.027
WO_3	4.60	40.98	0.043
Bi_2O_3	3.31	17.54	0.043
CW	23.88	25.72	0.148
CB	6.75	34.44	0.056
WB	3.85	39.93	0.029
WCB	21.73	29.22	0.151

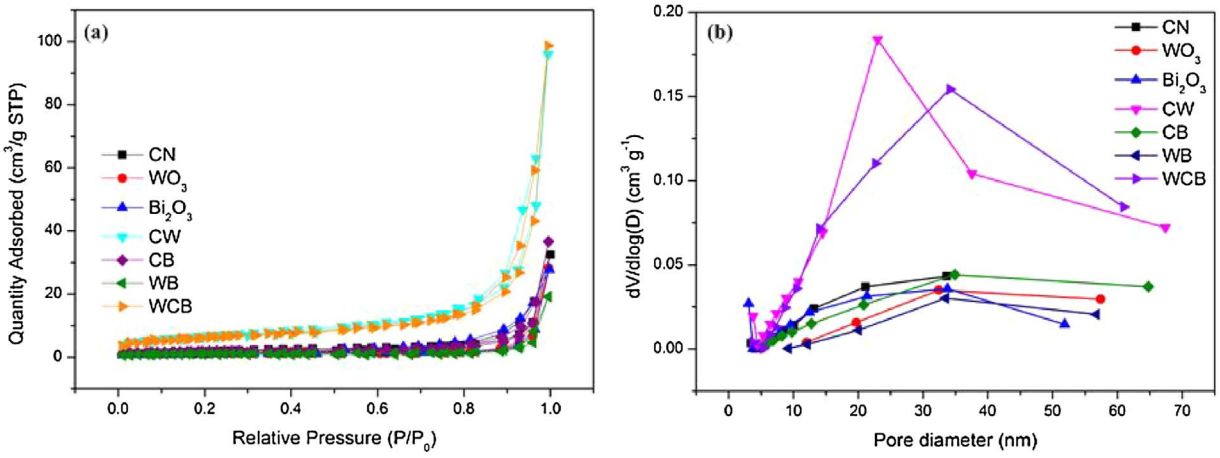

Fig. 4. N_2 adsorption–desorption isotherms (a) and the corresponding pore size distribution (b) of the as-prepared samples.

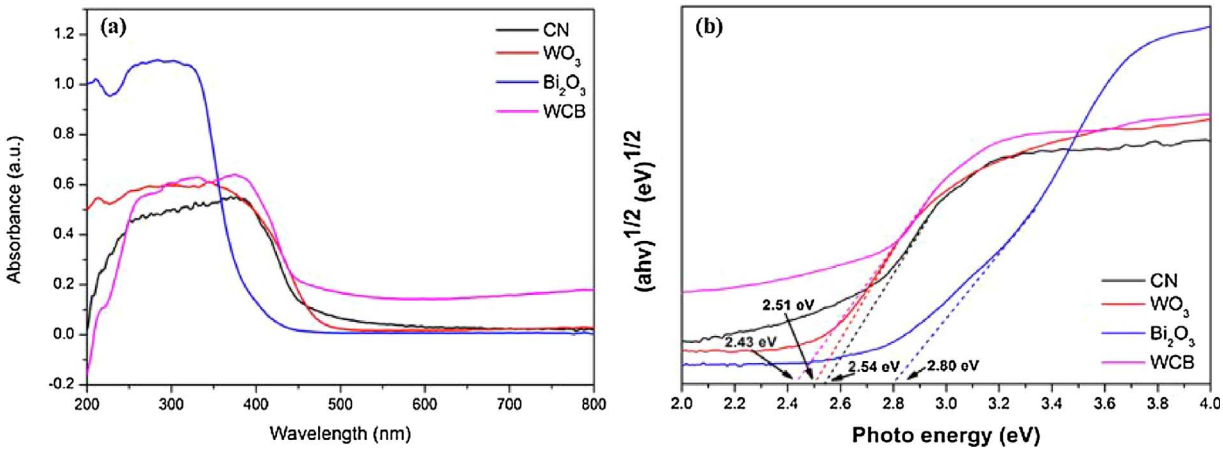

Fig. 5. UV–vis spectrum (a) and the bandgap of g-C_3N_4, WO_3, Bi_2O_3 and WCB.

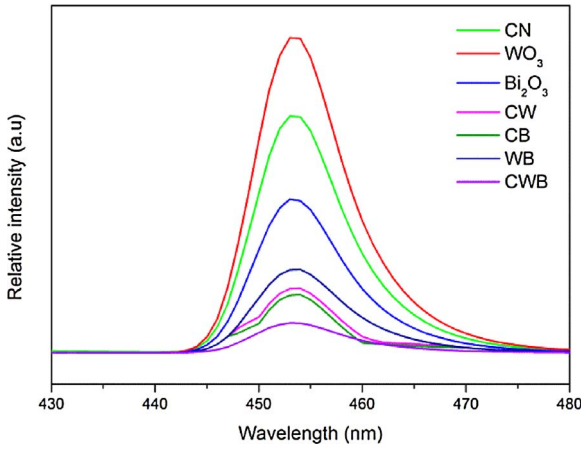

Fig. 6. Photoluminescence spectra of the as-prepared samples.

Bi_2O_3 and WCB at an excitation wavelength of 350 nm. All the single samples have strong emissions centered around 445–470 nm due to the recombination of electron–hole pairs. Obviously, the WCB heterostructures show significantly dropped PL intensity when compared with the pure samples and the binary composites, which suggests that the introduction of WO_3 nanoparticles and Bi_2O_3 sphere on the surface of g-C_3N_4 can decelerate the recombination rate of photogenerated electron–hole charges.

3.5. Photocatalytic activity and stability evaluation

The photocatalytic activity of the as-prepared samples were evaluated by photodegradation of TC under visible light irradiation. TC can only be slightly degraded without a photocatalyst, indicating that TC is a stable molecule and that the photolysis process can be ignored (Fig. 7a). The photocatalytic activities of the as-prepared single, binary and ternary samples have been investigated by the TC degradation reaction. The concentration of TC decreased gradually as the exposure time increased for all samples. As displayed in Fig. 7a, the WCB composite displayed much better photocatalytic activities than that of pure g-C_3N_4, WO_3, Bi_2O_3 and their binary composites under visible-light irradiation ($\lambda > 420$ nm). They were in the order of WCB > CW > CB > WB > Bi_2O_3 > g-C_3N_4 > WO_3. The pure WO_3 displayed the lowest TC removal efficiency of only ca. 7.17% under visible light irradiation for 60 min due to its poor visible light absorption capability and fast electron-hole recombination. While, g-C_3N_4 and Bi_2O_3 have exhibited the degradation efficiency of about 22.1% and 28.61%, respectively. It is expected that when WO_3 or Bi_2O_3 is combined with g-C_3N_4, the photocatalytic activity is enhanced. The TC removal of CW and CB were 48.54% and 44.53% under the same conditions, respectively. The enhance photocatalytic activities can be caused by the formation of a heterojunction or Z-scheme junction at the interface between the different components, which is consistent with the previous reports [6,32]. When WO_3 and Bi_2O_3 were both deposited on the surface of g-C_3N_4, WCB nanocomposite exhibited the highest degradation efficiency (ca. 80.2%) under the same condition. The enhanced photocatalytic activity of WCB was caused by improved visible light absorption, increased surface area and enhanced separation efficiency of photo-generated electron-hole charges which was confirmed by UV–vis spectrum, N_2 adsorption–desorption isotherms and PL emission spectra, respectively. The results indicated the formation of WCB ternary composite and the synergistic effects between each component, which drastically enhanced the photocatalytic performance.

The reaction kinetics of WCB samples for photodegradation of TC are modeled by the pseudo-first-order kinetics model: $\ln(C/C_0) = -kt$, where C_0 and C is the initial concentration and instant concentration at reaction time t, and k is the rate constant. As shown in Fig. S2, the corresponding plot of $\ln(C/C_0) \sim t$ exhibits a good linearity. The values of the rate constant k for all the samples are exhibited in Fig. 7b in a more intuitive way. It can be found that WCB displayed the highest rate constant. The k value for TC degradation over WCB (0.02367 min^{-1}) sample is about 5.84, 20.06, 4.28, 2.16, 2.20 and 3.26 times higher than that of g-C_3N_4 (0.00405 min^{-1}), WO_3 (0.00118 min^{-1}), Bi_2O_3 (0.00553 min^{-1}), CW (0.01098 min^{-1}), CB (0.01077 min^{-1}) and WB (0.00726 min^{-1}), respectively. These results demonstrated that the formation of WO_3/g-C_3N_4/Bi_2O_3 composite could greatly promote the photocatalytic activity of g-C_3N_4.

Total organic carbon (TOC) analysis is an efficient method to evaluate the mineralization rate of TC. Fig. 8 displayed the TOC removal rate of the as-prepared photocatalysts after 120 min irradiation. It was obvious that WCB exhibited a mineralization rate of 69.3% which was much higher than that of pure CN (18.2%), WO_3 (11.3%) and Bi_2O_3 (22.6%). Moreover, the mineralization rate of WCB was also much higher than the binary composites described above.

The lifetime of the photocatalyst is a major parameter of the catalytic process, so it is essential to evaluate the stability of the catalyst for practical application. To evaluate the stability of the as-prepared photocatalysts, the TC degradation experiments of the WCB composite were repeated up to five times under the same conditions. For each cycle, the photocatalyst was collected by centrifugation, washing and drying before next run. As depicted in Fig. 9a, the photocatalytic activity of the WCB sample has no apparent deactivation even after five successive recycles for the degradation of TC (only about 8.2% loss) under visible light irradiation. Furthermore, XRD patterns of the WCB composite before and after 8th run cycle in Fig. 9b indicated that the phase and

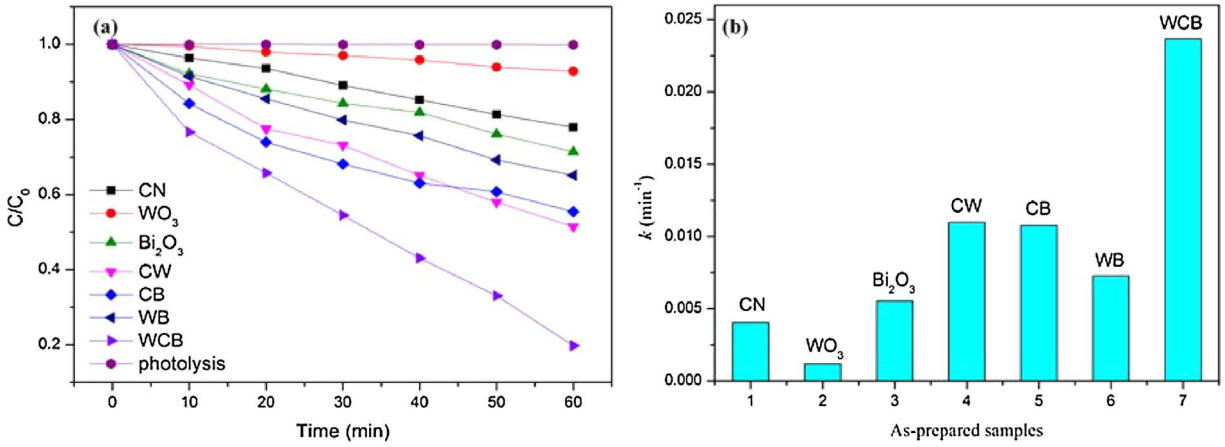

Fig. 7. (a) The photocatalytic activities of as-prepared samples for TC degradation under visible-light (λ > 420 nm); (b) The apparent rate constants for TC degradation.

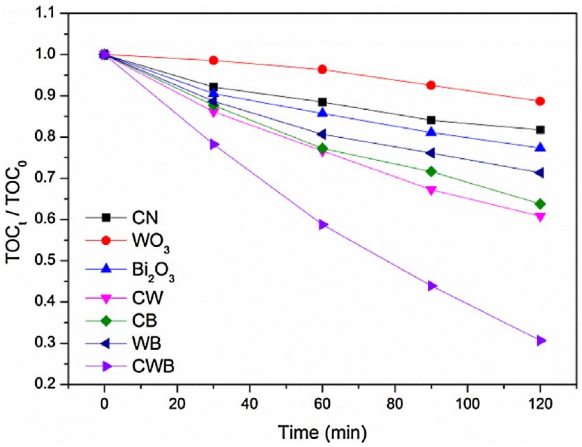

Fig. 8. TOC removal by the as-prepared samples.

structure of the recycled WCB composite had almost no obvious discrepancy compared with the unirradiated one. The results revealed its excellent stability and great potential value in environmental purification.

3.6. Photocatalytic mechanism

To investigate the predominant active species for TC degradation in the photocatalytic reaction process and understand the reaction mechanism in depth. The free radical and hole trapping experiments over WCB composite are first implemented, in which, triethanolamine (TEA) [3], 1,4-benzoquinone (BQ) [65] and isopropanol (IPA) [66] were employed as the scavengers of holes (h^+), superoxide radicals ($\cdot O_2^-$) and hydroxyl radicals ($\cdot OH$), respectively. The concentrations of these scavengers in the photocatalytic system were 1 mM. As displayed in Fig. 10, the degradation efficiency of TC are 80.2% when no scavenger was added. Notably, the TC removal are inhibited to 35.1%, 46.6% and 59.1% when BQ, TEA and IPA are added into reaction solution, respectively. It is obvious that $\cdot O_2^-$, h^+, and $\cdot OH$ are the predominant active species for the WO_3/g-C_3N_4/Bi_2O_3 sample. The order of the influence is $\cdot O_2^- > h^+ > \cdot OH$.

To further confirm the presence of $\cdot OH$ and $\cdot O_2^-$ radicals in the WCB photocatalytic reaction systems under visible light, the ESR spin-trap technique was performed. As depicted in Fig. 11a, under dark conditions, no obvious peak could be found for both DMPO-$\cdot O_2^-$ and DMPO-$\cdot OH$. However, when the photocatalysts were exposed to visible light, the characteristic peaks of DMPO-$\cdot O_2^-$ were observed in the methanol dispersion of WCB and the signal enhanced with the irradiation time, which implying the $\cdot O_2^-$ radical species were produced. Moreover, the typical characteristic peaks of DMPO-$\cdot OH$ adducts (Fig. 11b) were also observed, indicating that the $\cdot OH$ radicals also presented in WCB reaction systems.

In order to explain the photocatalytic degradation mechanism, the VB and CB edge positions of WO_3, g-C_3N_4 and Bi_2O_3 should be confirmed. The potentials of the VB and CB can be calculated according to the following equations:

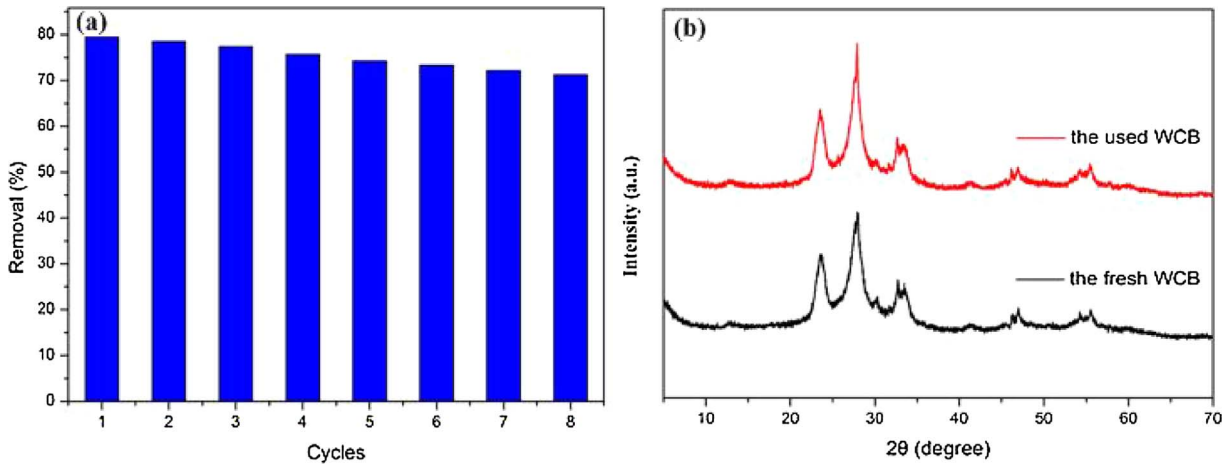

Fig. 9. (a) The repeated photocatalytic experiments of WCB photocatalyst for degradation of TC under visible light irradiation; (b) The XRD pattern of the WCB sample after 8th run cycle photocatalytic experiments.

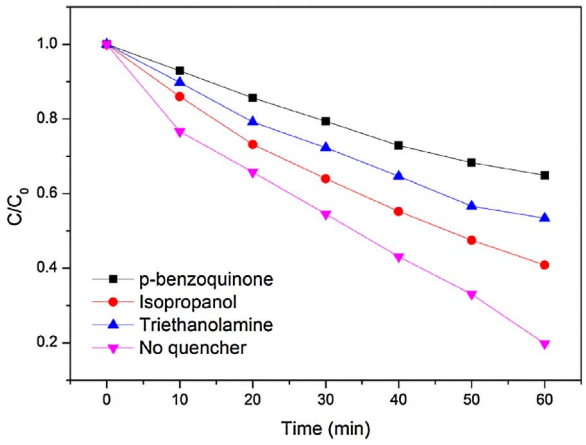

Fig. 10. The species trapping experiments for degradation of TC over CWB photocatalysts under visible light irradiation.

$$E_{cB} = X - E^e - \frac{1}{2}E_g \quad (2)$$

$$E_{vB} = E_{cB} + E_g \quad (3)$$

where X is the electronegativity of the semiconductor, E^e is the energy of free electrons on the hydrogen scale (about 4.5 eV). According to the above formulas, the CB potentials of WO_3, g-C_3N_4 and Bi_2O_3 were calculated to be 0.83 eV, −1.05 eV and 0.34 eV, respectively, and the VB potentials were 3.34 eV, 1.49 eV and 3.14 eV, respectively.

According to the band gap structures of WO_3, g-C_3N_4 and Bi_2O_3, the separation processes of photoexcited electron–hole could be exhibited in Fig. 12a and b, respectively. There are two possible charge separation ways for WO_3/g-C_3N_4/Bi_2O_3 composite. In detail, one is the traditional double-transfer mechanism and the other is Z-scheme mechanism. As shown in Fig. 12a, the electrons in the CB of g-C_3N_4 will migrate to the CB of Bi_2O_3 and then transfer to the CB of WO_3 if the charge carriers of WCB transfer according to the double-transfer mechanism. While, the holes in the VB of WO_3 will migrate to the VB of Bi_2O_3 and final transfer to the VB of g-C_3N_4. As a result, the electrons will accumulate to the CB of WO_3 and the holes will gather to the VB of g-C_3N_4. If this is true, the accumulated electrons on the CB of WO_3 can not reduce O_2 to form $\cdot O_2^-$ radicals due to the CB of WO_3 is more positive than the potential of $O_2/\cdot O_2^-$ (−0.33 eV vs. NHE) [54]. Moreover, the holes of g-C_3N_4 can not oxidize OH^- or H_2O to give ·OH due to the VB potential of g-C_3N_4 is lower than the standard redox potential of $OH^-/\cdot OH$ (2.40 eV vs. NHE) and $H_2O/\cdot OH$ (2.72 eV vs. NHE) [32,38]. However, the trapping experiment and ESR results indicated that $\cdot O_2^-$, h^+, and ·OH are the predominant active species for the WO_3/g-C_3N_4/Bi_2O_3 photocatalytic system. Therefore, the separation and transfer process of the photogenerated electron–hole charges should not follow the common heterojunction process in Fig. 12a.

According to the above discussion and the experimental results, a possible direct solid-state Z-scheme mechanism was proposed. As schematized in Fig. 12b, g-C_3N_4, WO_3 and Bi_2O_3 can produce photoinduced electron–hole pairs under visible light irradiation. Then, the photoinduced electrons in the CB of WO_3 would transfer and recombine with the holes in the VB of g-C_3N_4 [6]. Simultaneously, the photogenerated electrons in the CB of Bi_2O_3 also combined with the holes in the VB of g-C_3N_4 [32]. The migration of charge carrier can result in the electron accumulating in the CB of g-C_3N_4 (-1.05 ev), and the holes retained in the VB of WO_3 (3.34 eV) and Bi_2O_3 (3.14 eV), respectively. Therefore, the photoexcited electrons that remained and accumulated in the CB of g-C_3N_4 could be trapped by O_2 to yield $\cdot O_2^-$. Simultaneously, the holes left in VB of WO_3 and Bi_2O_3 have enough energy to degrade TC or oxidize H_2O to form ·OH radicals. The active radical ($\cdot O_2^-$ and ·OH) subsequently participate in the removal of TC. Therefore, it can be concluded that the photocatalytic reaction of prepared WO_3/g-C_3N_4/Bi_2O_3 composite follows a direct solid-state Z-scheme mechanism, which not only can accelerate the separation and transfer of photogenerated charges but also can retain the strong redox ability for efficient degradation of TC.

4. Conclusions

In summary, the novel direct solid state dual Z-scheme WO_3/g-C_3N_4/Bi_2O_3 was successfully synthesized by one step co-calcination stratage. The obtained WO_3/g-C_3N_4/Bi_2O_3 composites exhibit more efficient photocatalytic performance for TC degradation than pure g-C_3N_4, WO_3, Bi_2O_3 and their binary composites under the visible light irradiation. The enhanced photocatalytic activity of WO_3/g-C_3N_4/Bi_2O_3 composite can be ascribed to improved visible light absorption, increased surface area and enhanced separation efficiency of photo-generated electron-hole pairs. The radical trapping experiment and ESR analysis confirmed that the active species $\cdot O_2^-$, h^+ and ·OH were produced in the WO_3/g-C_3N_4/Bi_2O_3 photocatalytic system. The mechanism analysis demonstrated that the charges transfer of WO_3/g-C_3N_4/Bi_2O_3 composite followed a direct solid-state dual Z-scheme but not heterojunction.

Acknowledgements

The authors gratefully acknowledge the financial support provided by the National Natural Science Foundation of China (No. 51739004,

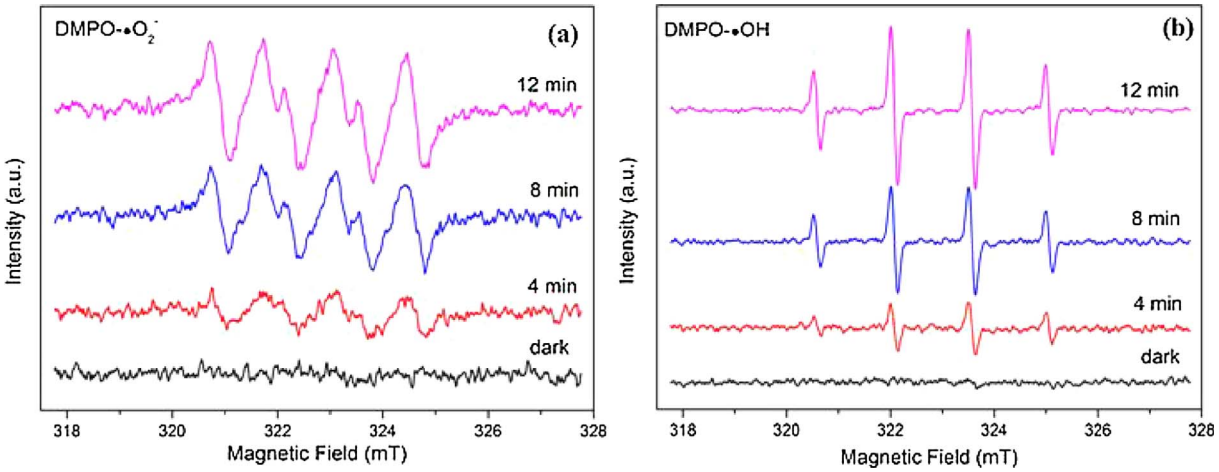

Fig. 11. DMPO spin-trapping ESR spectra with WCB sample in methanol dispersion (for DMPO-$\cdot O_2^-$) and in aqueous dispersion (for DMPO-·OH) under visible light irradiation.

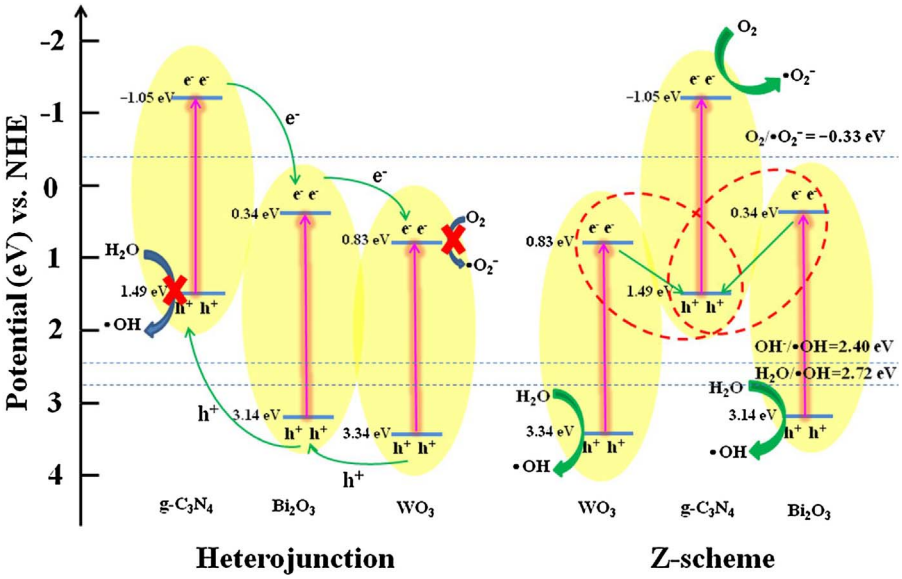

Fig. 12. Schematic diagram for the possible charge separation of WO_3/g-C_3N_4/Bi_2O_3, (a) Heterojunction, (b) Z-scheme.

No. 21776066, No. 51521006, No. 71431006, No. 51708195) and Key research and development project of Hunan Province, China (No. 2016SK2015).

Appendix A. Supplementary data

Supplementary data associated with this article can be found, in the online version, at https://doi.org/10.1016/j.apcatb.2018.01.042.

References

[1] L. Jiang, X. Yuan, Y. Pan, J. Liang, G. Zeng, Z. Wu, H. Wang, Doping of graphitic carbon nitride for photocatalysis: a reveiw, Appl. Catal. B Environ. 217 (2017) 388–406.
[2] L. Jiang, X. Yuan, G. Zeng, X. Chen, Z. Wu, J. Liang, J. Zhang, H. Wang, H. Wang, Phosphorus- and sulfur-codoped g-C3N4: facile preparation, mechanism insight, and application as e ffi cient photocatalyst for tetracycline and methyl orange degradation under visible light irradiation, ACS sustain, Chem. Eng. 5 (2017) 5831–5841.
[3] H. Wang, X. Yuan, H. Wang, X. Chen, Z. Wu, L. Jiang, W. Xiong, G. Zeng, Facile synthesis of Sb2S3/ultrathin g-C3N4 sheets heterostructures embedded with g-C3N4 quantum dots with enhanced NIR-light photocatalytic performance, Appl. Catal. B Environ. 193 (2016) 36–46.
[4] J. Liang, J. Liu, X. Yuan, H. Dong, G. Zeng, H. Wu, H. Wang, J. Liu, S. Hua, S. Zhang, Z. Yu, X. He, Y. He, Facile synthesis of alumina-decorated multi-walled carbon nanotubes for simultaneous adsorption of cadmium ion and trichloroethylene, Chem. Eng. J. 273 (2015) 101–110.
[5] J. Liang, X. Li, Z. Yu, G. Zeng, Y. Luo, L. Jiang, Z. Yang, Y. Qian, H. Wu, Amorphous MnO2 modified biochar derived from aerobically composted swine manure for adsorption of Pb(II) and Cd(II), ACS Sustain. Chem. Eng. 5 (2017) 5049–5058.
[6] S. Chen, Y. Hu, S. Meng, X. Fu, Study on the separation mechanisms of photo-generated electrons and holes for composite photocatalysts g-C3N4-WO3, Appl. Catal. B Environ. 150–151 (150) (2014) 564–573.
[7] X.L. Yin, J. Liu, W.J. Jiang, X. Zhang, J.S. Hu, L.J. Wan, Urchin-like Au@CdS/WO3 Micro/Nano heterostructure as a visible-light driven photocatalyst for efficient hydrogen generation, Chem. Commun. 51 (2015) 13842–13845.
[8] Z. Wu, X. Yuan, J. Zhang, H. Wang, L. Jiang, G. Zeng, Photocatalytic decontamination of wastewater containing organic dyes by metal-organic frameworks and their derivatives, ChemCatChem (2016) 41–64.
[9] X. Yuan, H. Wang, Y. Wu, X. Chen, G. Zeng, L. Leng, C. Zhang, A novel SnS2–MgFe2O4/reduced graphene oxide flower-like photocatalyst: solvothermal synthesis, characterization and improved visible-light photocatalytic activity, Catal. Commun. 61 (2015) 62–66.
[10] F. Le Formal, S.R. Pendlebury, M. Cornuz, S.D. Tilley, M. Gra, J.R. Durrant, Back electron-hole recombination in hematite photoanodes for water splitting, J. Am. Chem. Soc. 136 (2014) 2564–2574.
[11] D.J. Martin, N. Umezawa, X. Chen, J. Ye, J. Tang, Facet engineered Ag3PO4 for efficient water photooxidation, Energy Environ. Sci. 6 (2013) 3380.
[12] W.K. Jo, T.S. Natarajan, Influence of TiO2 morphology on the photocatalytic efficiency of direct Z-scheme g-C3N4/TiO2 photocatalysts for isoniazid degradation, Chem. Eng. J. 281 (2015) 549–565.
[13] Y.P. Yuan, L.S. Yin, S.W. Cao, G.S. Xu, C.H. Li, C. Xue, Improving photocatalytic hydrogen production of metal-organic framework UiO-66 octahedrons by dye-sensitization, Appl. Catal. B Environ. 168–169 (168) (2015) 572–576.
[14] L. Ye, D. Wang, S. Chen, Fabrication and enhanced photoelectrochemical performance of moS2/S-doped g-C3N4 heterojunction film, ACS Appl. Mater. Interfaces 8 (2016) 5280–5289.
[15] K. Zhang, Y. Liu, J. Deng, S. Xie, X. Zhao, J. Yang, Z. Han, H. Dai, Co–Pd/BiVO4. High-performance photocatalysts for the degradation of phenol under visible light irradiation, Appl. Catal. B Environ. 224 (2018) 350–359.
[16] Y. Zhu, Q. Ling, Y. Liu, H. Wang, Y. Zhu, Photocatalytic performance of BiPO4 nanorods adjusted via defects, Appl. Catal. B Environ. 187 (2016) 204–211.
[17] Z. Wu, X. Yuan, G. Zeng, L. Jiang, H. Zhong, Y. Xie, H. Wang, X. Chen, H. Wang, Highly efficient photocatalytic activity and mechanism of Yb3+/Tm3+ codoped In2S3 from ultraviolet to near infrared light towards chromium (VI) reduction and rhodamine B oxydative degradation, Appl. Catal. B Environ. 225 (2018) 8–21.
[18] D. Yin, L. Zhang, X. Cao, Z. Chen, J. Tang, Y. Liu, T. Zhang, M. Wu, Preparation of a novel nanocomposite NaLuF4:Gd, Yb, Tm@SiO2@Ag@TiO2 with high photocatalytic activity driven by simulated solar light, Dalt. Trans. 45 (2016) 1467–1475.
[19] H. Wang, L. Zhang, Z. Chen, J. Hu, S. Li, Z. Wang, J. Liu, X. Wang, Semiconductor heterojunction photocatalysts: design, construction, and photocatalytic performances, Chem. Soc. Rev. 43 (2014) 5234–5244.
[20] M. Reza Gholipour, C.-T. Dinh, F. Béland, T.-O. Do, Nanocomposite heterojunctions as sunlight-driven photocatalysts for hydrogen production from water splitting, Nanoscale 7 (2015) 8187–8208.
[21] K. Zhang, Y. Liu, J. Deng, S. Xie, H. Lin, X. Zhao, J. Yang, Z. Han, H. Dai, Fe2O3/3DOM BiVO4, High-performance photocatalysts for the visible light-driven degradation of 4-nitrophenol, Appl. Catal. B Environ. 202 (2017) 569–579.
[22] F. Chen, Q. Yang, Y. Wang, J. Zhao, D. Wang, X. Li, Z. Guo, H. Wang, Y. Deng, C. Niu, G. Zeng, Novel ternary heterojunction photcocatalyst of Ag nanoparticles and g-C3N4 nanosheets co-modified BiVO4 for wider spectrum visible-light photocatalytic degradation of refractory pollutant, Appl. Catal. B Environ. 205 (2017) 133–147.
[23] P. Zhou, J. Yu, M. Jaroniec, All-solid-state Z-scheme photocatalytic systems, Adv. Mater. 26 (2014) 4920–4935.
[24] A. Kudo, Z-scheme photocatalyst systems for water splitting under visible light irradiation, MRS Bull. 36 (2011) 32–38.
[25] X. Yuan, L. Jiang, X. Chen, L. Leng, H. Wang, Z. Wu, T. Xiong, J. Liang, G. Zeng, Highly efficient visible-light-induced photoactivity of Z-scheme Ag2CO3/Ag/WO3 photocatalysts for organic pollutant degradation, Environ. Sci. Nano 4 (2017) 2175–2185.
[26] Q. Wang, Y. Li, T. Hisatomi, M. Nakabayashi, N. Shibata, J. Kubota, K. Domen, Z-scheme water splitting using particulate semiconductors immobilized onto metal layers for efficient electron relay, J. Catal. 328 (2015) 308–315.
[27] J. Yan, H. Wu, H. Chen, Y. Zhang, F. Zhang, S.F. Liu, Fabrication of TiO2/C3N4 heterostructure for enhanced photocatalytic Z-scheme overall water splitting, Appl. Catal. B Environ. 191 (2016) 130–137.
[28] Y. Sasaki, A. Iwase, H. Kato, A. Kudo, The effect of co-catalyst for Z-scheme photocatalysis systems with an Fe3+/Fe2+ electron mediator on overall water splitting under visible light irradiation, J. Catal. 259 (2008) 133–137.
[29] W.K. Jo, N.C.S. Selvam, Z-scheme CdS/g-C3N4 composites with RGO as an electron mediator for efficient photocatalytic H2 production and pollutant degradation, Chem. Eng. J. 317 (2017) 913–924.
[30] D. Ma, J. Wu, M. Gao, Y. Xin, C. Chai, Enhanced debromination and degradation of 2,4-dibromophenol by an Z-scheme Bi2MoO6/CNTs/g-C3N4 visible light photocatalyst, Chem. Eng. J. 316 (2017) 461–470.
[31] N. Tian, H. Huang, Y. He, Y. Guo, T. Zhang, Y. Zhang, Mediator-free direct Z-scheme photocatalytic system: biVO4/g-C3N4 organic-inorganic hybrid photocatalyst with highly efficient visible-light-induced photocatalytic activity, Dalt. Trans. 44 (2015) 4297–4307.

[32] J. Zhang, Y. Hu, X. Jiang, S. Chen, S. Meng, X. Fu, Design of a direct Z-scheme photocatalyst: preparation and characterization of Bi2O3/g-C3N4 with high visible light activity, J. Hazard. Mater. 280 (2014) 713–722.
[33] Y. Deng, L. Tang, G. Zeng, J. Wang, Y. Zhou, J. Wang, J. Tang, Y. Liu, B. Peng, F. Chen, Facile fabrication of a direct Z-scheme Ag2CrO4/g-C3N4 photocatalyst with enhanced visible light photocatalytic activity, J. Mol. Catal. A Chem. 421 (2016) 209–221.
[34] J. Zhu, P. Xiao, H. Li, S.A.C. Carabineiro, Graphitic carbon nitride: synthesis, properties, and applications in catalysis, ACS Appl. Mater. Interfaces 6 (2014) 16449–16465.
[35] W.J. Ong, L.L. Tan, Y.H. Ng, S.T. Yong, S.P. Chai, Graphitic carbon nitride (g-C3N4)-based photocatalysts for artificial photosynthesis and environmental remediation: are we a step closer to achieving sustainability? Chem. Rev. 116 (2016) 7159–7329.
[36] Z. Zhao, Y. Sun, F. Dong, Graphitic carbon nitride based nanocomposites: a review, Nanoscale 7 (2014) 15–37.
[37] L. Jiang, X. Yuan, G. Zeng, Z. Wu, J. Liang, X. Chen, L. Leng, H. Wang, H. Wang, Metal-free efficient photocatalyst for stable visible-light photocatalytic degradation of refractory pollutant, Appl. Catal. B Environ. 221 (2018) 715–725.
[38] Y. Hong, Y. Jiang, C. Li, W. Fan, X. Yan, M. Yan, W. Shi, In-situ synthesis of direct solid-state Z-scheme V2O5/g-C3N4 heterojunctions with enhanced visible light efficiency in photocatalytic degradation of pollutants, Appl. Catal. B Environ. 180 (2016) 663–673.
[39] G. Mamba, A.K. Mishra, Graphitic carbon nitride (g-C3N4) nanocomposites: a new and exciting generation of visible light driven photocatalysts for environmental pollution remediation, Appl. Catal. B Environ. 198 (2016) 347–377.
[40] S. Cao, J. Low, J. Yu, M. Jaroniec, Polymeric photocatalysts based on graphitic carbon nitride, Adv. Mater. 27 (2015) 2150–2176.
[41] N. Tian, H.W. Huang, C.Y. Liu, F. Dong, T.R. Zhang, X. Du, S.X. Yu, Y.H. Zhang, In situ co-pyrolysis fabrication of CeO2/g-C3N4 n–n type heterojunction for synchronously promoting photo-induced oxidation and reduction properties, J. Mater. Chem. A 3 (2015) 17120–17129.
[42] J.C. Wang, H.C. Yao, Z.Y. Fan, L. Zhang, J.S. Wang, S.Q. Zang, Z.J. Li, Indirect Z-scheme biOI/g-C3N4 photocatalysts with enhanced photoreduction CO2 activity under visible light irradiation, ACS Appl. Mater. Interfaces 8 (2016) 3765–3775.
[43] Y. He, L. Zhang, B. Teng, M. Fan, New application of Z scheme ag3PO4/g-C3N4 composite in converting CO2 to fuel, Environ. Sci. Technol. 49 (2015) 649–656.
[44] L. Shao, D. Jiang, P. Xiao, L. Zhu, S. Meng, M. Chen, Enhancement of g-C3N4 nanosheets photocatalysis by synergistic interaction of ZnS microsphere and RGO inducing multistep charge transfer, Appl. Catal. B Environ. 198 (2016) 200–210.
[45] D. Lu, H. Wang, X. Zhao, K.K. Kondamareddy, J. Ding, C. Li, P. Fang, Highly efficient visible-light-induced photoactivity of Z-scheme g-C3N4/Ag/MoS2 ternary photocatalysts for organic pollutant degradation and production of hydrogen, ACS Sustain. Chem. Eng. 5 (2017) 1436–1445.
[46] F. Wu, X. Li, W. Liu, S. Zhang, Highly enhanced photocatalytic degradation of methylene blue over the indirect all-solid-state Z-scheme g-C3N4-RGO-TiO2 nanoheterojunctions, Appl. Surf. Sci. 405 (2017) 60–70.
[47] W.K. Jo, T.S. Natarajan, Fabrication and efficient visible light photocatalytic properties of novel zinc indium sulfide (ZnIn2S4) –graphitic carbon nitride (g-C3N4)/bismuth vanadate (BiVO4) nanorod-based ternary nanocomposites with enhanced charge separation via Z-scheme transfe, J. Colloid Interface Sci. 482 (2016) 58–72.
[48] L. Cui, X. Ding, Y. Wang, H. Shi, L. Huang, Y. Zuo, S. Kang, Facile preparation of Z-scheme WO3/g-C3N4 composite photocatalyst with enhanced photocatalytic performance under visible light, Appl. Surf. Sci. 391 (2017) 202–210.
[49] J. Ding, Q. Liu, Z. Zhang, X. Liu, J. Zhao, S. Cheng, B. Zong, W.L. Dai, Carbon nitride nanosheets decorated with WO3 nanorods: ultrasonic-assisted facile synthesis and catalytic application in the green manufacture of dialdehydes, Appl. Catal. B Environ. 165 (2015) 511–518.
[50] M.A. Gondal, A.A. Adesida, S.G. Rashid, S. Shi, R. Khan, Z.H. Yamani, K. Shen, Q. Xu, Z.S. Seddigi, X. Chang, Preparation of WO3/g-C3N4 composites and their enhanced photodegradation of contaminants in aqueous solution under visible light irradiation, React. Kinet. Mech. Catal. (2014) 357–367.
[51] J. Lu, Y. Wang, F. Liu, L. Zhang, S. Chai, Fabrication of a direct Z-scheme type WO3/Ag3PO4 composite photocatalyst with enhanced visible-light photocatalytic performances, Appl. Surf. Sci. 393 (2017) 180–190.
[52] F. Dong, Z. Zhao, T. Xiong, Z. Ni, W. Zhang, Y. Sun, W.-K. Ho, In situ construction of g-C3N4/g-C3N4 metal-free heterojunction for enhanced visible-light photocatalysis, ACS Appl. Mater. Interfaces 5 (2013) 11392–11401.
[53] W. Chen, T.Y. Liu, T. Huang, X. Liu, X. Yang, Novel mesoporous P-doped graphitic carbon nitride nanosheets coupled with ZnIn2S4 nanosheets as efficient visible light driven heterostructures with remarkably enhanced photo-reduction activity, Nanoscale 8 (2016) 3711–3719.
[54] J. Wang, L. Tang, G. Zeng, Y. Liu, Y. Zhou, Y. Deng, J. Wang, B. Peng, Plasmonic Bi metal deposition and g-C3N4 coating on Bi2WO6 microspheres for efficient visible-light photocatalysis, ACS Sustain. Chem. Eng. 5 (2017) 1062–1072.
[55] M. Yan, Y. Wu, F. Zhu, Y. Hua, W. Shi, The fabrication of a novel Ag3VO4/WO3 heterojunction with enhanced visible light efficiency in the photocatalytic degradation of TC, Phys. Chem. Chem. Phys. 18 (2016) 3308–3315.
[56] Y. Yan, Z. Zhou, X. Zhao, J. Zhou, A controlled anion exchange strategy to synthesize core-shell bismuth oxide/bismuth sulfide hollow heterostructures with enhanced visible-light photocatalytic activity, J. Colloid Interface Sci. 435 (2014) 91–98.
[57] T. Wang, W. Quan, D. Jiang, L. Chen, D. Li, S. Meng, M. Chen, Synthesis of redox-mediator-free direct Z-scheme AgI/WO3 nanocomposite photocatalysts for the degradation of tetracycline with enhanced photocatalytic activity, Chem. Eng. J. 300 (2016) 280–290.
[58] X. Yang, F. Qian, G. Zou, M. Li, J. Lu, Y. Li, M. Bao, Facile fabrication of acidified g-C3N4/g-C3N44 hybrids with enhanced photocatalysis performance under visible light irradiation, Appl. Catal. B Environ. 193 (2016) 22–35.
[59] H. Wang, X. Yuan, Y. Wu, G. Zeng, X. Chen, L. Leng, H. Li, Synthesis and applications of novel graphitic carbon nitride/metal-organic frameworks mesoporous photocatalyst for dyes removal, Appl. Catal. B Environ. 174–175 (174) (2015) 445–454.
[60] L. Huang, H. Xu, Y. Li, H. Li, X. Cheng, J. Xia, Y. Xu, G. Cai, Visible-light-induced WO3/g-C3N4 composites with enhanced photocatalytic activity, Dalton Trans. 42 (2013) 8606–8616.
[61] Z. Jiang, K. Qian, C. Zhu, H. Sun, W. Wan, J. Xie, H. Li, P.K. Wong, S. Yuan, Carbon nitride coupled with CdS-TiO2 nanodots as 2D/0D ternary composite with enhanced photocatalytic H2 evolution: a novel efficient three-level electron transfer process, Appl. Catal. B Environ. 210 (2017) 194–204.
[62] J. Di, J. Xia, M. Ji, B. Wang, S. Yin, Q. Zhang, Z. Chen, H. Li, Advanced photocatalytic performance of graphene-like BN modified BiOBr flower-like materials for the removal of pollutants and mechanism insight, Appl. Catal. B Environ. 183 (2016) 254–262.
[63] D. Liu, Z. Jiang, C. Zhu, K. Qian, Z. Wu, J. Xie, Graphene-analogue BN-modified microspherical BiOI photocatalysts driven by visible light, Dalt. Trans. 45 (2016) 2505–2516.
[64] Y. Huang, W. Fan, B. Long, H. Li, F. Zhao, Z. Liu, Y. Tong, H. Ji, Visible light Bi2S3/Bi2O3/Bi2O2CO3 photocatalyst for effective degradation of organic pollutions, Appl. Catal. B Environ. 185 (2016) 68–76.
[65] Y. Liu, X. Yuan, H. Wang, X. Chen, S. Gu, Q. Jiang, Z. Wu, L. Jiang, Y. Wu, G. Zeng, Novel visible light-induced g-C3N4-Sb2S3/Sb4O5Cl2 composite photocatalysts for efficient degradation of methyl orange, Catal. Commun. 70 (2015) 17–20.
[66] Z. Wu, X. Yuan, H. Wang, Z. Wu, L. Jiang, Facile synthesis of a novel full-spectrum-responsive Co2.67S4 nanoparticles for UV-, vis- and NIR-driven photocatalysis, Appl. Catal. B Environ. 202 (2017) 104–111.